



HAL
open science

Experimental study and micromechanical modelling of the effective elastic properties of Fe–TiB₂ composites

Khaoula Dorhmi, Katell Derrien, Zehoua Hadjem-Hamouche, Léo Morin, Frédéric Bonnet, Jean-Pierre Chevalier

► To cite this version:

Khaoula Dorhmi, Katell Derrien, Zehoua Hadjem-Hamouche, Léo Morin, Frédéric Bonnet, et al.. Experimental study and micromechanical modelling of the effective elastic properties of Fe–TiB₂ composites. *Composite Structures*, 2021, 272, pp.114122. 10.1016/j.compstruct.2021.114122 . hal-03287409

HAL Id: hal-03287409

<https://hal.science/hal-03287409>

Submitted on 15 Jul 2021

HAL is a multi-disciplinary open access archive for the deposit and dissemination of scientific research documents, whether they are published or not. The documents may come from teaching and research institutions in France or abroad, or from public or private research centers.

L'archive ouverte pluridisciplinaire **HAL**, est destinée au dépôt et à la diffusion de documents scientifiques de niveau recherche, publiés ou non, émanant des établissements d'enseignement et de recherche français ou étrangers, des laboratoires publics ou privés.

Experimental study and micromechanical modelling of the effective elastic properties of Fe–TiB₂ composites

Khaoula Dorhmi^a, Katell Derrien^a, Zehoua Hadjem-Hamouche^a, Léo Morin^{a,*}, Frédéric Bonnet^b, Jean-Pierre Chevalier^a

^aPIMM, Arts et Metiers Institute of Technology, CNRS, Cnam, HESAM University, 151 boulevard de l'Hopital, 75013 Paris, France

^bArcelorMittal Research, voie Romaine-BP30320, 57283 Maizières-les-Metz Cedex, France

A B S T R A C T

Keywords:

Fe–TiB₂ composites
Homogenization
Effective properties
FFT-based simulations
Mori–Tanaka

The aim of this paper is to investigate the effective properties of Fe–TiB₂ composites obtained after hot or cold rolling. The elastic moduli of both hot and cold rolled composites are measured experimentally using several methods. Microstructure analyses based on SEM observations are performed to characterize the distribution of particles and cracks, and are then used to generate 3D representative microstructures using the RSA method. This allows the numerical determination of the overall elastic behavior of Fe–TiB₂ composites using full-field FFT-based simulations. In addition, Young's moduli of the hot rolled Fe–TiB₂ composites are also determined analytically using the mean-field homogenization scheme of Mori–Tanaka. The elastic properties determined experimentally, analytically and numerically are in a good agreement. Overall, a significant improvement of the specific stiffness in comparison to standard steels is achieved irrespective of the processing conditions.

1. Introduction

For over more than a decade, weight reduction for automotive structures has been a major driving force for research in high performance steels. For many components the main design criterion has been the yield strength, in order to support load without any irreversible (plastic) deformation. Much research has been carried out to optimize yield strength versus formability, leading to new generations of high strength steels, such as DP (dual phase) and TRIP (transformation-induced plasticity) steels. With these steels, weight reduction has been achieved by reducing the thickness of components, which leads naturally to a decrease in stiffness. In applications where the design criterion is the stiffness, other alternative materials are thus needed.

Metal Matrix Composites (MMC) are particularly interesting for stiffness design criteria because a significant increase of the stiffness can be achieved if the reinforcing particles have a higher value of Young's modulus than that of the matrix [26]. In particular, Fe–TiB₂ composites have attracted substantial interest, since TiB₂ has a high Young's modulus and substantially lower density than steel. Much work has focused on the manufacturing process, synthesis, microstructure analysis [3,42,51], physical and mechanical properties [8,24,28,4,43], and damage mechanisms [11,20,25,48,10,50,14,9,49].

The interest of the Fe–TiB₂ composites studied here is both the specific manufacturing process and the improved mechanical properties of these steel composites. Titanium diboride “TiB₂” is covalent and has been used as a reinforcement for several composites, especially for aluminum and steels. The crystal structure of TiB₂ is hexagonal and is composed of titanium atoms in a hexagonal lattice and boron atoms in a triangular lattice. It has a very high melting point (around 3000°C [40,7]). It is particularly attractive due to its high hardness [39], its chemical stability, electrical and thermal conductive character, as well as its mechanical properties. Indeed it has a transverse isotropic elastic behavior which is generally approximated by an isotropic behavior with a very high elastic modulus $E = 583$ GPa [38]. Thus, as reinforcements, TiB₂ particles are often considered as the best for steel matrix composites, thanks to their mechanical and physical properties; in addition to their mechanical properties, the lightweight of TiB₂ particles helps Fe–TiB₂ MMC to have a lower density (ρ) than steel and hence a substantially higher specific stiffness (E/ρ).

Previous microstructures of Fe–TiB₂ composites showed the presence of two families of particles [24], large primary particles with hexagonal section and small eutectic particles; a particle volume fraction of about 13% led to an increase of the specific stiffness of about 15% compared to standard steels. It was also shown that plastic flow

* Corresponding author.

E-mail address: leo.morin@ensam.eu (L. Morin).

is inhomogeneous in the Fe matrix and that particle fracture is the predominant damage mechanism with almost no debonded particles during deformation [24,25].

Recently, improvements in continuous casting of this composite steel, achieved by modifications of the composition and the solidification rate, have led to a significantly finer particle distribution. After casting, the Fe-TiB₂ products obtained are processed either by (i) hot rolling or (ii) hot rolling followed by cold rolling (which will be simply termed as cold rolling throughout the paper, for simplicity), to obtain the desired sheet thickness required. Then, both undergo a recrystallization annealing.

The understanding of the effect of microstructure and processing on the elastic properties of metal-matrix composites is of great interest in applications where stiffness is considered as primary design criterion. In the case of Fe-TiB₂ composites, it appears necessary to quantify precisely their elastic properties after processing or forming. Indeed, the process of cold rolling is expected to induce damage, in the form of particle cracking or decohesion of the particles/matrix interfaces, which will ultimately decrease the overall stiffness due to the presence of micro-voids [14].

Several methods allow to estimate the elastic properties of composites:

- *Experimentally*, several techniques can be used to measure Young's moduli of metallic alloys, such as (i) static methods through tensile tests with high resolution strain measurement and (ii) dynamic tests based on flexural resonance method. These methods provide valuable macroscopic values of elastic moduli which can be, in general, measured with uncertainties of 1–2% [29].
- The elastic properties of composites can be alternatively investigated by *micromechanical modelling*, which consists in the determination of the homogenized properties based on the statistical distribution of inclusions in terms of their morphology, sizes and volume fractions. The generation of random representative microstructures, based on Scanning Electron Microscopy (SEM) observations and image analyses, can be performed by several methods [47] such as (i) collective rearrangement inspired by molecular dynamics which allows to achieve high volume fraction of inclusions (50 to 70% depending on the shape of the particles) and (ii) random sequential adsorption (RSA) algorithm which is efficient for composites containing low volume fraction of inclusions (less than 30%). The reconstructed microstructures are then used as an input of a micromechanical analysis which can be performed by several methods:
 - Mean-field approaches of homogenization, based on Mori-Tanaka's homogenization model, provide an analytical estimate of the macroscopic elasticity tensor based on the morphology, volume fraction and local behavior of the phases [34,6,1]. This method is generally used for heterogeneous materials with a volume fraction of particles that does not exceed 30% and is adapted to composites reinforced with particles [21,44].
 - Full-field simulations, based on the finite-element method (FEM) or Fast Fourier Transforms (FFT), allow the local and overall mechanical fields of a heterogeneous material to be computed. The FFT-based method of [36] is particularly interesting for numerical homogenization because (i) calculations are directly performed from microstructures obtained either from SEM, tomography or image reconstruction, without any meshing operations, (ii) it relies on the computational complexity of fast Fourier transforms which makes the method very efficient and faster than FEM and (iii) periodic boundary conditions are built-in, which makes the method suitable to compute the effective properties, in contrast with the finite element method which requires some additional pre-processing on the opposite RVE boundaries [37,18,45]. Several accelerated

schemes [17,31,33] have been developed to improve the low convergence rate of the basic scheme [36] in the case of highly contrasted materials. This method, which in most cases provides macroscopic results that are close to that predicted by mean-field approaches [21–23,25], permits to take into consideration microstructural details such as cracks [19].

The aim of this paper is to investigate experimentally, analytically and numerically, the effect of hot and cold rolling on the effective properties of new Fe-TiB₂ composites obtained by continuous casting. The characterization of the new Fe-TiB₂ composites is of particular interest in order to assess the effect of the microstructure (after rolling) on the overall elastic properties. The novelty of the approach considered in this work is that it consists in investigating the effective elastic properties of Fe-TiB₂ composites by combining experimental measures and a micromechanical modelling based on microstructure analysis and reconstruction. The advantages of this homogenization-based approach are that (i) it unravels the effect of the microstructure (such as particle shape and cracks) on the macroscopic properties and (ii) it can be used as a numerical tool to design optimal microstructures tailoring mechanical properties.

The paper is organized as follows. In Section 2, a microstructure analysis is performed in order to extract the essential features of Fe-TiB₂ composites. The elastic moduli of hot rolled and cold rolled Fe-TiB₂ composites are determined experimentally in Section 3. In Section 4, representative microstructures are reconstructed from SEM image analysis. Analytical and numerical approaches of homogenization are applied in Section 5 to the determination of the overall elastic properties of Fe-TiB₂ composites. Finally, in Section 6 the competition between particle aspect ratio and crystallographic anisotropy is investigated numerically.

2. Material and microstructure analysis

The reference manufacturing process of Fe-TiB₂ composites of this study was developed by ArcelorMittal [5]. These composites, designed for their high specific stiffness (E/ρ), are obtained by *in situ* precipitation of TiB₂ particles during eutectic solidification. This process leads to very clean and particularly strong matrix/reinforcement interfaces [8,28].

The manufacturing process of Fe-TiB₂ composites has been modified recently in order to refine the microstructure and homogenize the size of TiB₂ particles. Significant fractions of TiB₂ reinforcements (10–25% by volume) can be reached through the control of the chemical composition of the composite, while the size of the reinforcements can be widely optimized through the solidification rate of the material. After continuous casting, slabs of Fe-TiB₂ are either hot or cold rolled, and both are subjected to recrystallization annealing at 800 °C for 25 min (4 min of temperature rise and 21 min of holding time).

The hypereutectic composition of Fe-Ti-B steel studied here (see Table 1 for the composition) allows a fine microstructure with a uniform and homogeneous reinforcements distribution in the matrix to be obtained. The obtained microstructure, illustrated by Fig. 1, shows a ferritic matrix (light contrast) reinforced with particles elongated in the rolling direction (dark contrast). Two types of TiB₂ particles are present in the ferritic matrix: primary hexagonal particles, formed before eutectic transformation, and eutectic ones. The sizes and shapes of primary and eutectic particles are close to each other and can be related to prolate spheroids elongated in the rolling direction.

The microstructure of the hot and cold rolled Fe-TiB₂ composites were also characterized by EBSD. The EBSD crystal orientations maps, performed on 1×1 mm² surfaces and represented in Fig. 2, reveal that the matrix exhibits equiaxed grains in the RD plane with a mean grain size of about 3 μm. A weak crystallographic texture is observed in the matrix. EBSD analysis of the material shows also the crystallographic texture of the particles: the transverse isotropic axis of the TiB₂ parti-

Table 1Chemical composition of the Fe-TiB₂ composite.

Element	C	Al	Cr	Mn	Ni	Si	Ti	B	P	Fe
Weight %	0.04	0.07	0.06	0.09	0.04	0.17	5.4	1.69	0.01	Bal.

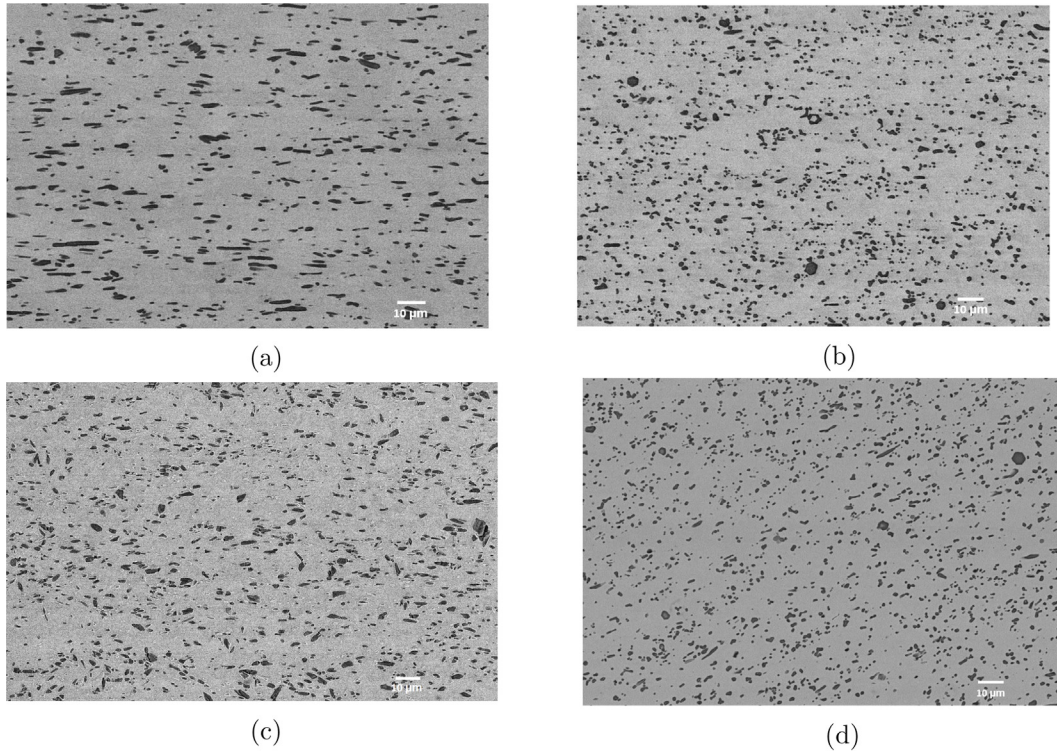


Fig. 1. SEM (image mode: BSE) micrographs of Fe-TiB₂ composite (TiB₂ particles appear with dark contrast). (a) Hot rolled, rolling direction, (b) Hot rolled, transverse direction (c) Cold rolled, rolling direction, (d) Cold rolled, transverse direction.

cles, represented by the axis c in Fig. 3, is mainly oriented along the rolling direction (see $\{0001\}$ pole figure in Fig. 2c).

The main feature of the hot rolling process is a redirection of TiB₂ particles in the rolling direction without any damage of the particles. In contrast, some particles were fractured during the cold rolling process. Overall, the average volume fraction of particles is the same for both composites (since this is the same material before the rolling process) and is of about $v_f = 10\%$. The following analysis will highlight the main differences between the microstructures of the hot and cold rolled composites.

The hot rolled composite A microstructure analysis has allowed the determination of a volume fraction for TiB₂ particles of about $v_f = 10\%$ in both the rolling direction (RD) and the transverse direction (TD). In addition, it has led to a classification of the particles according to their (i) aspect ratios in the rolling direction, and their (ii) diameters in the transverse direction, which is represented in Fig. 4.

First, the aspect ratios of the particles, represented in Fig. 4a, are classified from 1 to 6 and their distribution is relatively homogeneous in terms of volume fraction. The chosen group distribution is as follows: (a) 20% of the total volume fraction of particles for those having an aspect ratio of 1, (b) 27% for particles having an aspect ratio of 2, (c) 23% of particles having an aspect ratio of 3, and finally (d) an average of 30% of particles having an aspect ratio of 6. The distribution of the particle diameters, represented in Fig. 4b, reveals that there is a considerable lead of particles whose diameters are between 1 and 4 μm . Their average contribution to the volume fraction is around 92% and the contribution of the remaining particles is less than 8%. The chosen diameters that will represent all the particles are 2 and 3 μm .

The cold rolled composite After cold rolling, the distribution of the particles aspect ratios is the same than that after hot rolling. However, an important feature of the cold rolled composite is that it contains an average volume fraction of about 0.15% of voids in the form of cracks, which have been revealed by SEM observations after

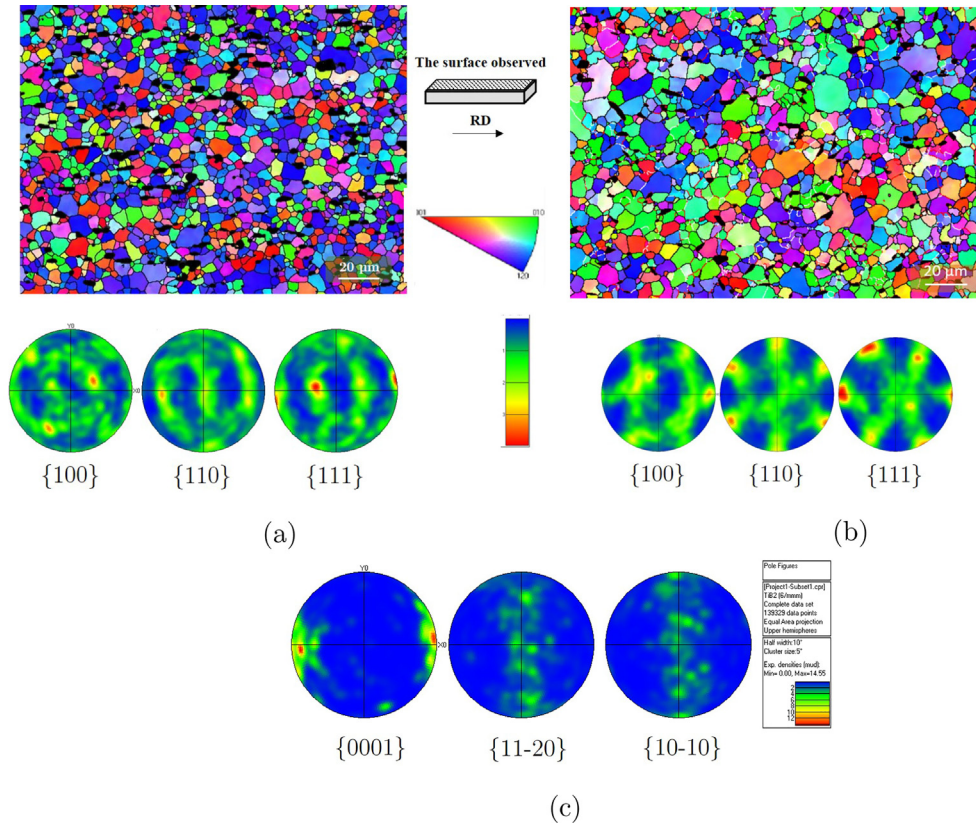


Fig. 2. EBSD mappings of grain orientations in the rolling direction plane; the dark phase corresponds to TiB_2 particles. (a) Cold rolled composite, (b) Hot rolled composite and (c) Crystallographic texture of the TiB_2 particles.

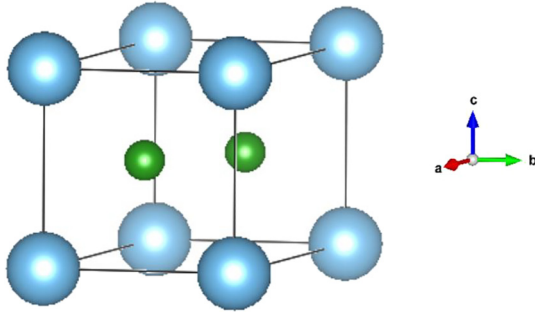


Fig. 3. Hexagonal crystal structure of titanium diboride.

electrolytic polishing. Details of the cold rolled microstructure, showing cracked particles and an example of one cracked particle in the cold rolled composite are given in Fig. 5.

3. Experimental determination of Young's moduli of Fe- TiB_2 composites

In this section, the Young's moduli of the cold rolled composite, in the rolling and transverse directions, will be measured experimentally using several static and dynamic methods and compared to those of the hot rolled composite measured by an extensometer.

3.1. Experimental methods

For tensile tests, a double-sided extensometer (class 0.2) from Zwick (Clipon) was used in parallel to a strain gauge HBM 1-LY41-3/350 applied on both faces of rectangular section test-piece. Valida-

tion of the gauge factor was previously done using a shunt resistor. Preloading at 80% of the yield strength is previously applied to eliminate bending artifacts and a minimum of two runs is applied (continuous loading/unloading cycles) at the same strength. Least squares fit is used on the linear elastic domain of loading to determine the Young's modulus. The measurement is considered valid only if the strain increment on opposite faces of the sample does not differ more than 3% as recommended in ASTM E111 [15] to eliminate all possible issue in relation to misalignment and out-of-plane bending defects. Three samples were characterized for each direction to provide statistic data.

In parallel, out-of-plane flexural resonance method on "free-free" beam test-piece with rectangular cross-section was used on the same samples [2]. The fundamental vibration frequency is determined by sweeping the frequency to detect resonance. Two wires are used to support the sample at the fundamental flexural node position and piezo-vibrators are applied on the sample just outside the nodal position to promote the vibration. The length and thickness of the samples are carefully measured and the density is determined with helium pycnometer to reach a higher level of accuracy. Since this method can be sensitive to surface finish and poor dimensional tolerance, the machining of the samples was carefully controlled to reduce scattering. For a rectangular section beam in flexure, Young's modulus is given by the formula

$$E = \left(\frac{48\pi^2}{\alpha^2} \right) \rho f^2 \frac{L^4}{t^2} T \frac{t}{L}, \quad (1)$$

where f is the resonance frequency, ρ the density, L the length (50 mm), l the height (9.8 mm) and t the thickness (from 1 to 2.5 mm) of the beam. Sample dimension was designed to avoid any overlapping of vibration mode ($L/t > 20$). In Eq. (1), the parameter α , which depends on experimental conditions, reads $\alpha = 22.37$ [13]. Finally, the parame-

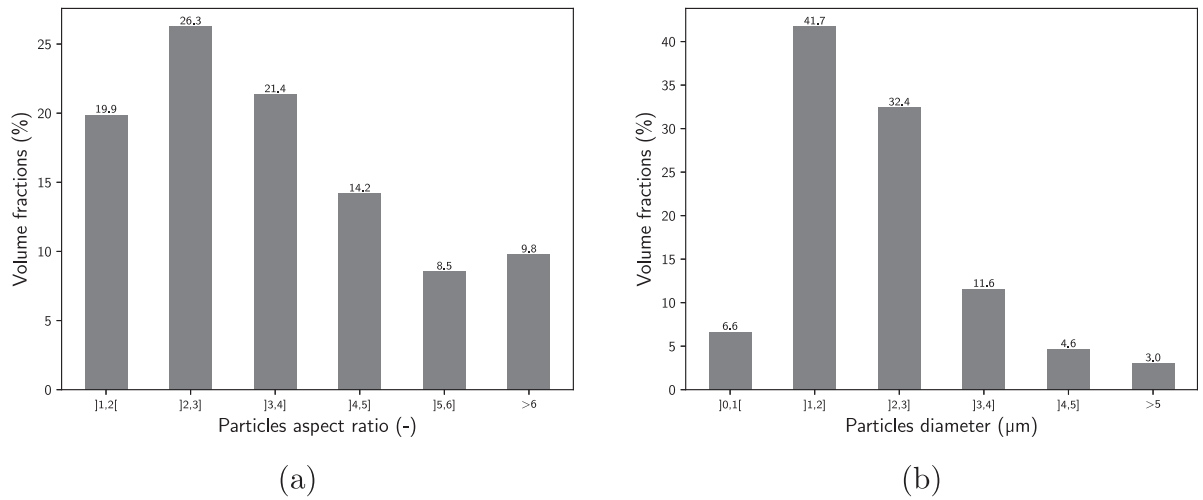


Fig. 4. Results of the SEM image analysis for the hot rolled Fe-TiB₂ composite. (a) Distribution of the particles' aspect ratios in the RD and (b) Distribution of the particles' diameters in the TD.

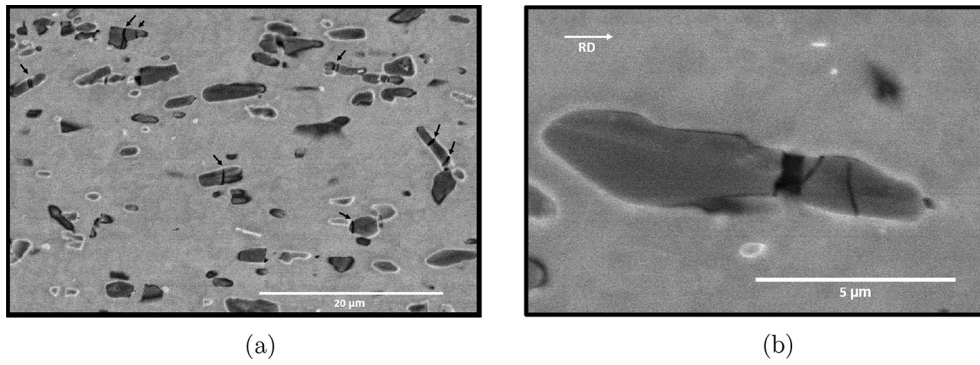


Fig. 5. SEM micrographs of Fe-TiB₂ cold rolled composite. (a) Typical microstructure showing several cracked particles in the cold rolled composite (indicated by arrows) and (b) Example of a cracked particle in the cold rolled composite.

ter T is a correcting factor close to 1 which integrates shear and rotary inertia [46,41]. For $L/t > 20$, T is given by the formula

$$T = 1 + 6.858 \frac{t^2}{L} \quad (2)$$

3.2. The cold rolled composite

Young's moduli of the cold rolled Fe-TiB₂ were measured in two directions (RD and TD) and the results are summarized in Table 2. Very similar results are obtained from the three methods presented in Section 3.1 (extensometer, strain gauges and resonance).

The elastic anisotropy is characterized by the non-dimensional (normalized) factor

$$a = \frac{|E_{RD} - E_{TD}|}{\frac{1}{2}(E_{RD} + E_{TD})} \quad (3)$$

which approximately represents the deviation from isotropy, where E_{RD} and E_{TD} respectively denote the longitudinal Young's modulus (in the rolling direction) and the transverse Young's modulus. (In the case of an isotropic material, the property $E_{RD} = E_{TD}$ holds which implies that $a = 0$; thus an increase of a characterizes an increase of the anisotropy).

A difference of about 10GPa between the longitudinal and transverse Young's moduli is obtained experimentally which leads to a deviation from isotropy a of about 0.042.

Table 2

Measures of Young's moduli of the cold rolled Fe-TiB₂ composite.

Experimental methods	Young's moduli (GPa)		Deviation from isotropy
	E_{RD}	E_{TD}	a
Extensometer	222.4	233.9	0.050
Strain gauge	223.5	230.2	0.030
Resonance	223.4	233.9	0.046

3.3. The hot rolled composite

Since it has been shown that the different methods used to measure the Young's moduli of cold rolled Fe-TiB₂ samples at room temperature gave almost the same results, we consider only the extensometer method for the hot rolled composite. The elastic properties are shown in Table 3.

Both longitudinal and transverse Young's moduli of the hot rolled composite are higher than that of the cold rolled composite. The rolling direction seems to be more affected by the cold rolling than the transverse direction. In that case, the deviation from isotropy a is of about 0.014 for the hot rolled composite which implies that the elastic anisotropy is a little less pronounced for the hot rolled composite.

Table 3Measures of Young's moduli of the hot rolled Fe-TiB₂ composite.

Experimental method	Young's moduli (GPa)		Deviation from isotropy
	E_{RD}	E_{TD}	a
Extensometer	230.4	233.7	0.014

4. Microstructure reconstruction from SEM images analysis

The statistical analysis made in Section 2 allows the classification of the particles into 5 groups. The average fraction of each group, diameters and aspect ratios of the particles are given in Table 4.

The sizes and volume fractions of particles of the cold rolled Fe-TiB₂ composite as well as the volume fraction of cracks in each group of particles are summarized in Table 5. The only difference between the hot and the cold rolled composite is the presence of some cracked particles in the cold rolled composite.

This 2D SEM image statistical analysis will serve as a basis to generate representative 3D microstructures of Fe-TiB₂ composites. 3D reconstructed microstructures are required because they allow building periodic RVEs which are needed for FFT-based calculations. Furthermore, all geometrical and topological parameters defining the microstructure can be easily modified in order to introduce porosity or cracks as observed in the case of cold rolled Fe-TiB₂, or to explore alternative distributions of constituents for material design.

Since the materials considered in this work (hot and cold rolled Fe-TiB₂ composites) contain low volume fraction of inclusions, the RSA method [47] is applied to generate all groups of spheroidal inclusions and cracks determined by image analysis (Tables 4 and 5). The RSA method consists in adding spheroidal particles sequentially into a cubic matrix:

1. A particle is generated in a randomly chosen position (x, y, z) where a spheroid (sound or cracked particle) is added. The cracks are generated in the plane normal to the rolling direction;
2. The new generated candidate is accepted only if it does not intercept any other particle generated previously. Otherwise it is removed;
3. The process is repeated until the desired number of particles (or cracks) and/or volume fraction is reached.

In order to reduce the microstructure generation time cost, the biggest particles are generated first and are followed by the smallest ones. Examples of reconstructed microstructures for both hot and cold rolled Fe-TiB₂ composites are provided in Fig. 6.

In practice, two types of discrepancies may occur during the generation of a microstructure: (i) voxelization artifacts related to the discretization of an ellipsoidal particle using (cubic) voxels and (ii) errors on the desired volume fraction since particles are added sequentially. In order to avoid voxelization artifacts, a sufficient number of voxels was considered for the smallest reconstructed TiB₂ particle as it is close to an ellipsoidal shape. Then, three RVE sizes ((128)³, (256)³ and (512)³) were studied in order to reduce the error made on the desired volume fraction. For the three RVE sizes considered, the same particle sizes (in voxel) were chosen, so an increase of the resolution (from (128)³ to (512)³) leads to an increase of the number of particles and thus allows the desired volume fraction of particles to be reached more accurately. In order to quantify the effect of the RVE size on the volume fraction, the relative error

$$e = \left| \frac{v_f^{\text{desired}} - v_f^{\text{reached}}}{v_f^{\text{desired}}} \right| \quad (4)$$

is calculated. The reconstruction of the microstructures is carried out on a 64-bit desktop computer with 128 GB RAM and an Intel Xeon Gold

6140 CPU, 2.30 GHz, Ubuntu 16.04 LTS. The CPU time and relative error e associated to the microstructure generations using the RSA method are given in Table 6 for each RVE resolution ((128)³, (256)³ and (512)³).

As expected, the CPU time and the number of the generated particles are the highest for the (512)³ discretization, for both the hot and the cold rolled composites. For the (128)³ discretization, the relative error on the volume fraction of the truly generated particles is the highest. Indeed, for a desired volume fraction $v_f = 10\%$, only $v_f = 9.1\%$ of particles are generated for the (128)³ discretization, while $v_f = 9.8\%$ and $v_f = 9.9\%$ of particles are reached for the (256)³ and (512)³ discretizations, respectively. The CPU time of the cold rolled composite is higher than the hot rolled one, merely because we have made the choice to generate the particles first, then add the cracks after.

5. Analytical and numerical modelling of the overall elastic properties of Fe-TiB₂ composites

5.1. Analytical and numerical approaches of homogenization for heterogeneous materials

Two methods for the determination of the overall elastic properties of heterogeneous materials are presented. The full-field FFT-based method is the main homogenization technique used here to obtain effective properties of the hot and cold rolled Fe-TiB₂ composites. The analytical homogenization method by the Mori-Tanaka's mean field approach will also be used to assess the numerical results obtained by the FFT-based method.

5.1.1. Analytical homogenization by mean field approaches

The Mori-Tanaka scheme [34] is a mean-field homogenization method for elastic properties, based on the Eshelby inclusion problem [16]. We investigate the overall behavior of a n -phases composite made of a matrix and $(n - 1)$ phases.

The stiffness tensors of the matrix and the remaining phases (particles for example) are respectively denoted by \mathbb{C}_0 and \mathbb{C}_r , and their volume fractions are respectively denoted by f_0 and f_r (with r ranging from 1 to $n - 1$). The macroscopic stiffness tensor of the composite, denoted by \mathbb{C}_{hom} , is given by

$$\mathbb{C}_{\text{hom}} = \left(\sum_{r=0}^{n-1} f_r \mathbb{C}_r : \mathbb{T}_r \right) : \left(\sum_{r=0}^{n-1} f_r \mathbb{T}_r \right)^{-1}. \quad (5)$$

In Eq. (5), the tensor \mathbb{T}_r is given by

$$\mathbb{T}_r = (\mathbb{I} + \mathbb{S}_r^{\text{Esh}} : \mathbb{C}_0^{-1} : (\mathbb{C}_r - \mathbb{C}_0))^{-1} \quad (6)$$

where $\mathbb{S}_r^{\text{Esh}}$ is the (classical) Eshelby tensor.

In the case of hot rolled Fe-TiB₂ composites, which are made of a matrix containing 5 groups of spheroidal particles, this mean-field homogenization method is naturally adapted. In the case of cold rolled Fe-TiB₂ composites, however, this method is not suitable due to the presence of cracks which are not accounted for by the original Mori-Tanaka's model. Therefore, full-field homogenization methods are considered hereafter to overcome the intrinsic limitations of Mori and Tanaka's scheme.

5.1.2. Numerical homogenization by full-field FFT-based calculations

In many cases, mean-field approaches cannot be used when the microstructures considered are too complex, as in the case of cold rolled Fe-TiB₂ composites due to the presence of cracks. In such case, it becomes necessary to rely on full-field simulations. The FFT-based method can notably be used to determine the effective properties of composites by applying the following procedure:

Table 4

Classification of the five groups (G1, G2, G3, G4 and G5) of particles in the hot rolled composite.

Group	G1	G2	G3	G4	G5
Diameter (μm)	2	3	3	3	2
Aspect ratio	6	3	2	1	1
Fraction of particles (%)	30	23	27	10	10
Volume fraction of particles (%)	3	2,3	2,7	1	1

Table 5

Classification of the five groups (G1, G2, G3, G4 and G5) of particles and cracks in the cold rolled composite.

Group	G1	G2	G3	G4	G5
Diameter (μm)	2	3	3	3	2
Aspect ratio	6	3	2	1	1
Fraction of particles (%)	30	23	27	10	10
Fraction of cracked particles (%)	45	40	30	30	30

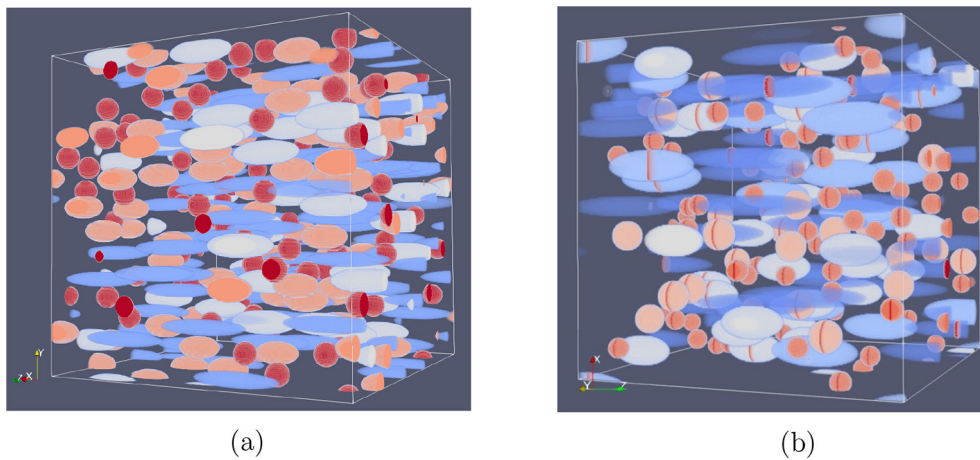


Fig. 6. Microstructure reconstruction of Fe-TiB₂ composite after SEM image analysis (RVE size = 512³ voxels). (a) Hot rolled composite and (b) Cold rolled composite.

Table 6

The CPU time required for RVE generation by RSA method, the number of the particles and the relative error on the generated volume fraction of particles in the case of $v_f = 10\%$, for hot and cold rolled Fe-TiB₂ composites, for the three discretizations considered.

RVE Size	CPU time (seconds)		Number of particles	e (%)
	Hot rolled	Cold rolled		
RSA-(128) ³	14.9	28.5	56	9
RSA-(256) ³	119.1	185.0	449	2
RSA-(512) ³	1097.2	1359.7	3595	1

1. Impose periodic boundary conditions at the edges of the RVE;
2. Apply the local behavior law corresponding to each constituent of the composite;
3. Solve for six loading conditions, by imposing only one non-zero component of the macroscopic stress tensor $\bar{\sigma}_{ij}$ to the RVE;
4. Compute the macroscopic strain tensor $\bar{\epsilon}$ by spatial averaging of the local strain tensor ϵ over the RVE;
5. Each independent equation of the overall elastic law $\bar{\sigma}_{ij} = C_{ijkl}\bar{\epsilon}_{kl}$ provides between one and three coefficients of the stiffness tensor C_{ijkl} for each macroscopic stress tensor $\bar{\sigma}_{ij}$;
6. Post-process to eventually compute global stress and strain, in the composite.

In practice, the augmented Lagrangian scheme is used for the calculations because of the high contrast between the mechanical properties of the matrix, particles and voids (in the form of cracks). The simulations are performed using the software Craft [36,31].

For the simulations, we consider the reconstructed microstructures using the procedure described in Section 4 based on SEM image analysis. For the microstructures of the hot rolled Fe-TiB₂ composite, the average volume fraction of reinforcements is about 10 %. In the case of cold rolled composites, there is an additional volume fraction of about 0.15 % of cracks (which decreases the volume fraction of the matrix).

In terms of the local behavior of the phases, an isotropic linear elastic behavior is considered for the ferritic matrix, which is characterized by a Young's modulus $E = 210$ GPa and a Poisson's ratio $\nu = 0.33$.

For the particles, the crystal structure of TiB_2 is hexagonal and composed of titanium atoms of hexagonal lattice and boron atoms of triangular lattice. Both are stacked alternately along the vertical axis c . (The local basis (a, b, c) is represented in Fig. 3). Thus, the spheroidal TiB_2 particles have a “transverse isotropic” behavior in the direction c , with transverse properties that are higher than their longitudinal ones. For the elastic behavior of the TiB_2 particles, we consider the experimental values of [38]; the stiffness tensor of the TiB_2 particles, expressed using Kelvin notation (see Appendix A for a description of the Kelvin notation for tensors) and denoted by $\hat{\mathbf{C}}_{\text{TiB}_2}$, reads in the local basis (a, b, c) :

$$\hat{\mathbf{C}}_{\text{TiB}_2} = \begin{pmatrix} 654.5 & 56.5 & 98.4 & 0 & 0 & 0 \\ 56.5 & 654.5 & 98.4 & 0 & 0 & 0 \\ 98.4 & 98.4 & 454.5 & 0 & 0 & 0 \\ 0 & 0 & 0 & 526.4 & 0 & 0 \\ 0 & 0 & 0 & 0 & 526.4 & 0 \\ 0 & 0 & 0 & 0 & 0 & 598 \end{pmatrix} \text{ (GPa)}. \quad (7)$$

In the following, the direction c will be supposed to coincide with the spheroidal axis of the particles, which is itself supposed to be aligned with the rolling direction. This axis will be denoted by x_3 by convenience.

5.2. Overall elastic properties of the hot and cold rolled composite

5.2.1. Representativeness of the calculations

First, we need to study the effect of the RVE resolution on the effective properties of the composite, in order to choose a suitable one. Three different RVE discretizations $((128)^3, (256)^3$ and $(512)^3$ voxels) are investigated and the CPU time, associated to one simulation using the numerical FFT-based method, is given in Table 7.

An increase of the RVE resolution naturally leads to an increase of the CPU time required to make one full computation of the elastic properties of both hot or cold rolled Fe–TiB₂ composites. Furthermore, we can notice that the calculations, in the case of cold rolled composites, require more CPU time due to the presence of cracks; indeed the infinite contrast in phases induced by cracks is known to increase the number of iterations in FFT-based calculations [36].

Then, it is necessary to perform a statistical analysis of the calculations in order to obtain representative results [52]. It should be noted that this statistical analysis is performed for a given RVE size; the results of the statistical analysis are independent of the volume fraction of particles (and thus the overall properties) but depend on the distribution of particles. As shown in Section 4, an increase of the RVE size leads to an increase of the number of particles and thus provides a more random distribution of particles, which is expected to improve the representativeness of the calculations. Due to the large number of particles generated randomly (see Table 6), the overall elasticity tensor determined numerically is expected to have a transverse isotropic behavior. The statistical analysis can thus be performed on the Young’s moduli in the rolling and transverse directions, respectively denoted by E_{RD} and E_{TD} and defined by

$$E_{RD} = \frac{1}{\hat{S}_{33}}, \quad E_{TD} = \frac{1}{\hat{S}_{11}}, \quad (8)$$

where $\hat{\mathbf{S}}$ is the overall compliance tensor. For a given resolution, n RVE are generated based on the microstructure reconstruction procedure described in Section 3, and used to compute the overall elastic properties. According to [21] (see also [27]), the number n of simulations is sufficient if the following inequality is verified:

$$\max(X_{RD}, X_{TD}) \leq 0.1\%, \quad X_{RD} = \frac{T_{1-\alpha}^{n-1} S_{E_{RD}}}{E_{RD} \sqrt{n}}, \quad X_{TD} = \frac{T_{1-\alpha}^{n-1} S_{E_{TD}}}{E_{TD} \sqrt{n}}.$$

Table 7

CPU time required to the computation of elastic properties by FFT-based method for hot and cold rolled Fe–TiB₂ composites, for three resolutions.

RVE Discretization	CPU time (seconds)	
	Hot rolled	Cold rolled
FFT-(128) ³	23.6	28.5
FFT-(256) ³	168.5	1870.8
FFT-(512) ³	1331.1	17882.7

In Eq. (9), $S_{E_{RD}}$ and $S_{E_{TD}}$ are estimates of the standard deviation of E_{RD} and E_{TD} , respectively, and T is the quantile of the student distribution with $n - 1$ degrees of freedom. Furthermore, the confidence level is generally set as $(1 - \alpha) = 0.95$ (see [21]).

The criterion defined by Eq. (9) is then applied for the three RVE discretizations considered $((128)^3, (256)^3$ and $(512)^3$) which allows the minimum number of calculations needed to achieve representativeness to be obtained. Convergence is reached after 4 calculations for the resolution of $(128)^3$, 3 calculations for the resolution of $(256)^3$ and 2 calculations for the resolution of $(512)^3$.

Thus, by taking into consideration (i) the CPU time (of particle generation and calculation), (ii) the error made on the volume fraction of particles (due to the generation method), and (iii) the number of calculations needed to obtain representative results, a discretization of $(256)^3$ is chosen for all calculations.

5.2.2. Effective properties of the hot rolled Fe–TiB₂ composite

The non-zero components of the overall stiffness tensor of the hot rolled Fe–TiB₂ composite, denoted by $\hat{\mathbf{C}}$ with the Kelvin notation, have been determined numerically using the FFT-based method and are given in Table 8. These coefficients approximately verify the relations $\hat{C}_{11} = \hat{C}_{22}, \hat{C}_{13} = \hat{C}_{23}, \hat{C}_{44} = \hat{C}_{55}$, and $\hat{C}_{66} = \hat{C}_{11} - \hat{C}_{12}$, which is expected since the overall behavior of the reconstructed hot rolled composite is isotropic transverse by construction (due to the random generation of the particles).

Then, the Young’s moduli in the rolling and transverse directions E_{RD} and E_{TD} (defined by Eq. (8)) determined numerically by the FFT method are given in Table 9, together with the analytical results given by the Mori–Tanaka scheme. The first observation is that the predicted elastic moduli obtained by the FFT-based method are in very good agreement with results provided by the Mori–Tanaka scheme and that the transverse elastic modulus (E_{TD}) is higher than the modulus in the rolling direction (E_{RD}).

The anisotropy of the overall behavior can be characterized by computing the distance between the (anisotropic) elasticity tensor and its closest isotropic tensor, allowing to define rigorously the notion of deviation from isotropy of tensors; this permits to extend to tensors the parameter a that was approximately introduced in Section (3.2) for the experimental data (see Eq. (3)). In order to characterize the deviation from isotropy of the macroscopic behavior, we first determine the elastic properties of its closest isotropic tensor (denoted by E_{iso} and ν_{iso}), which are given in Table 9. This was done using the Log-Euclidean distance of [32] (see also [35]) which is invariant by inversion of the stiffness tensor, allowing the determination of a unique closest isotropic tensor (see Appendix B). The distance between the anisotropic tensor determined either by FFT or Mori–Tanaka’s scheme, and its respective closest isotropic one, denoted by d_{in} , is also given in Table 9. Since the Log-Euclidean distance is related to the relative error between elasticity tensors (see [12]), the values obtained in both cases (roughly 0.018) confirm that the predicted elastic moduli of hot rolled Fe–TiB₂ composites are very close to isotropy. This unexpected overall isotropic behavior is related to a competition between the anisotropic behavior and the spheroidal shape of the particles (see [12]).

Table 8Average values of stiffness tensor coefficients obtained after FFT computations of the reconstructed hot rolled Fe–TiB₂

	Stiffness tensor coefficients in Kelvin notation (GPa)								
	\hat{C}_{11}	\hat{C}_{12}	\hat{C}_{13}	\hat{C}_{22}	\hat{C}_{23}	\hat{C}_{33}	\hat{C}_{44}	\hat{C}_{55}	\hat{C}_{66}
FFT-(256) ³	329.0	152.2	150.4	329.0	150.4	322.7	176.9	176.9	176.6

Table 9The Young's moduli in two directions (RD and TD), calculated by the FFT-based method and by the Mori–Tanaka scheme for the reconstructed hot rolled Fe–TiB₂ composite, as well as the associated closest isotropic tensor Young's modulus and the Log-Euclidean distance characterizing the deviation from isotropy.

	E_{RD} (GPa)	E_{TD} (GPa)	E_{iso} (GPa)	ν_{iso} (-)	d_{in}
FFT-(256) ³	228.6	232.7	232.0	0.32	0.018
Mori–Tanaka	228.6	232.4	232.0	0.32	0.018

Table 10Average values of stiffness tensor coefficients obtained after FFT computations of the reconstructed cold rolled Fe–TiB₂ composites

	Stiffness tensor coefficients in Kelvin notation (GPa)								
	\hat{C}_{11}	\hat{C}_{12}	\hat{C}_{13}	\hat{C}_{22}	\hat{C}_{23}	\hat{C}_{33}	\hat{C}_{44}	\hat{C}_{55}	\hat{C}_{66}
FFT-(256) ³	328.0	151.7	148.9	328.0	148.9	316.5	174.9	174.8	176.1

Table 11The Young's moduli in two directions (RD and TD), calculated by the FFT-based method for the reconstructed cold rolled Fe–TiB₂ composite, as well as the associated closest isotropic tensor Young's modulus and the Log-Euclidean distance characterizing the deviation from isotropy.

	E_{RD} (GPa)	E_{TD} (GPa)	E_{iso} (GPa)	ν_{iso} (-)	d_{in}
FFT-(256) ³	223.9	232.1	230.0	0.32	0.033

5.2.3. Effective properties of the cold rolled Fe–TiB₂ composite

The non-zero components of the overall stiffness tensor of the cold rolled Fe–TiB₂ composite are given in Table 10. As in the case of hot rolled composites, these coefficients approximately verify the relations $\hat{C}_{11} = \hat{C}_{22}$, $\hat{C}_{13} = \hat{C}_{23}$, $\hat{C}_{44} = \hat{C}_{55}$, and $\hat{C}_{66} = \hat{C}_{11} - \hat{C}_{12}$, which is expected since the overall behavior of the reconstructed cold rolled composite is isotropic transverse by construction because the cracks are generated randomly in the direction normal to the rolling direction.

The Young's modulus in the rolling and transverse directions, E_{RD} and E_{TD} , deduced from the overall stiffness tensor determiner numerically,¹ are given in Table 11. It is worth noting that the Young's modulus in the transverse direction is not affected by the presence of cracks while a significant decrease of the Young's modulus in the rolling direction is observed, in comparison with the hot rolled composite.

Again, the deviation from isotropy of the macroscopic stiffness tensor is characterized by the determination of its closest isotropic tensor, using as previously the Log-Euclidean distance. The elastic properties of the closest isotropic tensor (denoted by E_{iso} and ν_{iso}) and the distance d_{in} are given in Table 11. In the case of the cold rolled Fe–TiB₂ composite, the distance between the elasticity tensor determined numerically and its closest isotropic tensor (roughly 0.033) is higher than that obtained in the case of hot rolled ones (0.018); this implies that the presence of voids (in the form of cracks) decreases the overall isotropy of the composite. Moreover, the Young's modulus associated to the closest isotropy tensor of the cold rolled composite ($E_{iso} = 230.0$ GPa) is lower than that of the hot rolled composite ($E_{iso} = 232.0$ GPa). Thus, the effective properties, as well as the overall

¹ In that case, the Mori–Tanaka's predictions are not given since this does not take cracks into consideration.

Table 12Summary of the effective elastic properties of hot rolled and cold rolled FeTiB₂ composites.

	Hot rolled		Cold rolled	
	E_{RD} (GPa)	E_{TD} (GPa)	E_{RD} (GPa)	E_{TD} (GPa)
Experimental	230.4	233.7	223.1	232.6
FFT-(256) ³	228.6	232.7	223.9	232.1

isotropy of the hot rolled Fe–TiB₂ composites, decrease (slightly) after cold rolling.

6. Discussion

A summary of the effective elastic properties is given in Table 12. Overall, the Young's moduli determined numerically by FFT using representative microstructures reconstructed from SEM images are in good agreement with that measured experimentally for both hot rolled and cold rolled FeTiB₂ composites. Some comments are in order:

- In the case of hot rolled composites, the Young's moduli in the transverse direction appear to be very close to that in the rolling direction, which implies that the overall behavior is close to isotropy. This is confirmed by the values of the parameters characterizing the deviation from isotropy, $a = 0.014$ for the experimental results and $d_{in} = 0.018$ for the numerical results.
- In the case of cold rolled composites, a decrease of about 7.3 GPa of the longitudinal Young's modulus (E_{RD}) is observed in the experimental results, and of about 4.7 GPa in the numerical ones. A small decrease of the transverse Young's modulus (E_{TD}) is also observed. This loss of stiffness is associated with an increase of the deviation

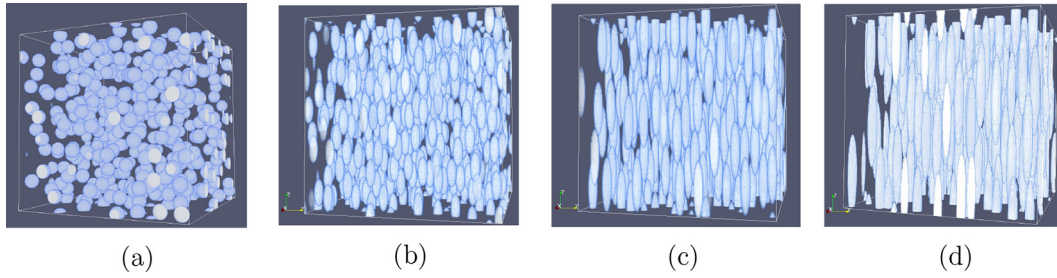


Fig. 7. Randomly generated spheroidal (prolate) particles with a volume fraction of 10%. (a) Aspect ratio of 1, (b) Aspect ratio of 3, (c) Aspect ratio of 6 and (d) Aspect ratio of 9.

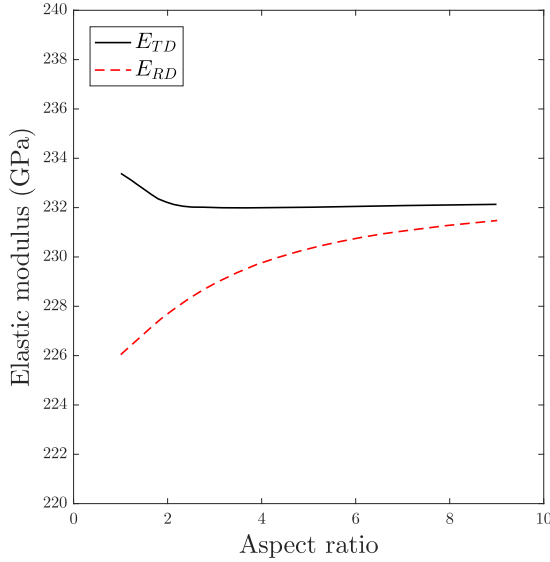


Fig. 8. Influence of the particles' aspect ratio on the moduli E_{TD} and E_{RD} .

from isotropy, with values $a = 0.042$ for the experimental results and $d_{in} = 0.033$ for the numerical results. Since an important fraction of cracks was observed in the cold rolled composite, the decrease of both the overall elastic properties and the overall isotropy is attributed to the presence of these cracks which have nucleated during the plastic deformation induced by cold rolling processing.

This modeling, based on microstructure reconstruction and statistical analysis, is a powerful tool to investigate the properties of composites. It can be notably used for material design by making changes in the microstructure in order to tailor mechanical properties. In the present case, it could be used to study the effect, on the effective properties of the Fe-TiB₂ composite, of several geometrical and morphological parameters related to the TiB₂ particles including volume fraction, misalignment of some particles and aspect ratios, among others.

Since the hot rolled Fe-TiB₂ composite exhibits a quasi-isotropic behavior, it is of interest to study numerically the effect of the TiB₂ particles aspect ratio on the deviation from isotropy. A simplified case with only one family of particles is considered in order to focus only on the aspect ratio. Several microstructures reinforced with 10% of ellipsoidal TiB₂ particles are thus randomly generated with different aspect ratios and some of them are represented in Fig. 7. The effect of the aspect ratio on the E_{TD} and E_{RD} is represented in Fig. 8, for a ferritic matrix with isotropic Young's modulus $E = 210$ GPa reinforced with a volume fraction of 10% of TiB₂ particles (whose behavior is

given by Eq. (7)). The gap between E_{TD} and E_{RD} is maximal when the aspect ratio is equal to 1. When the aspect ratio increases, the gap between E_{TD} and E_{RD} decreases. For an aspect ratio of about 20 the two moduli E_{TD} and E_{RD} becomes equal. The deviation from isotropy in Fe-TiB₂ composites is thus related to a subtle coupling between the intrinsic material anisotropy of the TiB₂ particles and the anisotropy induced by the aspect ratio of the particles.

7. Conclusion

The aim of this paper was to study, experimentally, analytically and numerically, the effective properties of hot and cold rolled Fe-TiB₂ composites whose microstructures have been recently refined.

First, the Young's moduli in the rolling and transverse directions of hot and cold rolled Fe-TiB₂ composites have been determined experimentally using several methods (extensometer, strain gauge and resonance). A small loss of stiffness is observed in cold rolled composites.

Then, a microstructure analysis of Fe-TiB₂ composites, based on SEM observations, has permitted to classify TiB₂ particles into five groups in terms of their diameters and aspect ratios in both composites as well as cracks in cold rolled composites. This classification has served as a basis to generate representative microstructures using the RSA method.

The generated microstructures were used to determine the overall elastic properties of the hot and cold rolled Fe-TiB₂ composites using analytical homogenization and numerical full-field FFT-based simulations. A good agreement is observed with the experimental results, which confirms that the damage induced by cold rolling degrades (moderately) the overall elastic properties of Fe-TiB₂ composites.

It is worth noting that the effective properties of both hot and cold rolled Fe-TiB₂ composites are still higher than that of standard steels, which still makes them good candidates in lightweight structures with stiffness as primary criterion. Since cold rolling induces a small decrease of the overall stiffness, it is expected that processes based on plastic deformation (such as forming) would also lead to decrease of the elastic properties. This implies that the effect of processing on the elastic properties must be carefully taken into account for MMC composites to be used in industrial applications.

Future developments of this work will concern (i) the study of the overall stiffness evolution of Fe-TiB₂ composites during plastic deformation (e.g. in tensile tests and forming processes) and (ii) the numerical prediction of the overall rigidity of industrial structural parts made of Fe-TiB₂ composites and obtained after forming, using the homogenization-based damage model developed by [14].

Declaration of Competing Interest

The authors declare that they have no known competing financial interests or personal relationships that could have appeared to influence the work reported in this paper.

Acknowledgments

This work is supported by the Carnot Institut Arts. The authors would like to thank P. Fort, from ArcelorMittal, who made it possible to carry out the Young's moduli measurements by the resonance method. Fruitful discussions with S. Berbenni, O. Castelnau, J. Genée, N. Gey, G. Gonzalez and V. Michel are gratefully acknowledged.

Appendix A. The Kelvin notation in elasticity

The tensorial elasticity law relates the second-order stress and strain tensors, respectively denoted by $\boldsymbol{\sigma}$ and $\boldsymbol{\varepsilon}$, through the linear relations

$$\boldsymbol{\sigma} = \mathbb{C} : \boldsymbol{\varepsilon}, \quad \boldsymbol{\varepsilon} = \mathbb{S} : \boldsymbol{\sigma}, \quad \mathbb{C} : \mathbb{S} = \mathbb{S} : \mathbb{C} = \mathbb{I}, \quad (\text{A.1})$$

where \mathbb{C} and \mathbb{S} respectively denote the fourth-order stiffness and compliance tensors, and \mathbb{I} is the fourth-order identity tensor. Elasticity tensors are positive-definite and possess minor and major symmetries

$$\begin{aligned} C_{ijkl} &= C_{jikl} = C_{ijlk}, & C_{ijkl} &= C_{klij}, \\ S_{ijkl} &= S_{jikl} = S_{ijlk}, & S_{ijkl} &= S_{klij}. \end{aligned}$$

The Kelvin notation in elasticity (see [30] for a comprehensive description of the Kelvin notation) is a very useful tool to express the tensorial elasticity law. Fourth-order elasticity tensors in three dimensions are equivalent to second-order tensors in six dimensions; the tensor \mathbb{C} can be represented by the 6×6 matrix $\hat{\mathbb{C}}$ defined by

$$\hat{\mathbb{C}} = \begin{pmatrix} C_{1111} & C_{1122} & C_{1133} & \sqrt{2}C_{1123} & \sqrt{2}C_{1113} & \sqrt{2}C_{1112} \\ C_{1122} & C_{2222} & C_{2233} & \sqrt{2}C_{2223} & \sqrt{2}C_{2213} & \sqrt{2}C_{2212} \\ C_{1133} & C_{2233} & C_{3333} & \sqrt{2}C_{3323} & \sqrt{2}C_{3313} & \sqrt{2}C_{3312} \\ \sqrt{2}C_{1123} & \sqrt{2}C_{2223} & \sqrt{2}C_{3323} & 2C_{2323} & 2C_{2313} & 2C_{2312} \\ \sqrt{2}C_{1113} & \sqrt{2}C_{2213} & \sqrt{2}C_{3313} & 2C_{2313} & 2C_{1313} & 2C_{1312} \\ \sqrt{2}C_{1112} & \sqrt{2}C_{2212} & \sqrt{2}C_{3312} & 2C_{2312} & 2C_{1312} & 2C_{1212} \end{pmatrix}. \quad (\text{A.2})$$

Second-order symmetric tensors in three dimensions are equivalent to vectors of six dimensions. Thus, the associated stress and strain vectors denoted $\hat{\boldsymbol{\sigma}}$ and $\hat{\boldsymbol{\varepsilon}}$ are given by

$$\hat{\boldsymbol{\sigma}} = \begin{pmatrix} \sigma_{11} \\ \sigma_{22} \\ \sigma_{33} \\ \sqrt{2}\sigma_{23} \\ \sqrt{2}\sigma_{13} \\ \sqrt{2}\sigma_{12} \end{pmatrix}, \quad \hat{\boldsymbol{\varepsilon}} = \begin{pmatrix} \varepsilon_{11} \\ \varepsilon_{22} \\ \varepsilon_{33} \\ \sqrt{2}\varepsilon_{23} \\ \sqrt{2}\varepsilon_{13} \\ \sqrt{2}\varepsilon_{12} \end{pmatrix}. \quad (\text{A.3})$$

The elasticity law can then be rewritten with the Kelvin notation as

$$\hat{\boldsymbol{\sigma}} = \hat{\mathbb{C}} \cdot \hat{\boldsymbol{\varepsilon}}, \quad \hat{\boldsymbol{\varepsilon}} = \hat{\mathbb{S}} \cdot \hat{\boldsymbol{\sigma}}, \quad \hat{\mathbb{C}} \cdot \hat{\mathbb{S}} = \hat{\mathbb{I}}_6, \quad (\text{A.4})$$

where $\hat{\mathbb{I}}_6$ is the 6×6 identity matrix.

Appendix B. The closest isotropic tensor to an arbitrary elasticity tensor

In many applications, it is of interest to determine the closest isotropic tensor to an arbitrary elasticity tensor. The problem considered reduces to the minimization of the distance between the given tensor \mathbb{C} and the closest isotropic tensor \mathbb{C}_{iso} sought. It has been shown in [32,35] that the most suitable distance function for tensors, in this problem, is the Log-Euclidean function because it is invariant by inversion.

We are thus looking for the closest isotropic tensor \mathbb{C}_{iso} of a given tensor \mathbb{C} , which is necessarily of the form

$$\mathbb{C}_{\text{iso}} = 3\kappa\mathbb{J} + 2\mu\mathbb{K}, \quad (\text{B.1})$$

where κ and μ are respectively the bulk modulus and shear modulus; \mathbb{J} and \mathbb{K} are linearly independent isotropic tensors defined by

$$\mathbb{J} = \frac{1}{3}\mathbb{I}_3 \otimes \mathbb{I}_3, \quad \mathbb{K} = \mathbb{I} - \mathbb{J}, \quad (\text{B.2})$$

where \mathbb{I}_3 is the second-order identity tensor. Using the Kelvin notation (the tensors \mathbb{C} and \mathbb{C}_{iso} are respectively represented by their 6×6 matrices $\hat{\mathbb{C}}$ and $\hat{\mathbb{C}}_{\text{iso}}$ as shown in Appendix A), the closest isotropic tensor $\hat{\mathbb{C}}_{\text{iso}}$ is that which minimizes the Log-Euclidean distance [32]

$$d_{\text{in}}(\hat{\mathbb{C}}, \hat{\mathbb{C}}_{\text{iso}}) = \left\| \ln(\hat{\mathbb{C}}) - \ln(\hat{\mathbb{C}}_{\text{iso}}) \right\|, \quad (\text{B.3})$$

where $\|\cdot\|$ is the classical Euclidean norm and $\ln(\cdot)$ is the logarithm function of a 6×6 matrix (see [32,35]). The minimization of the distance (B.3) is unique and leads to the bulk modulus and shear modulus of the closest isotropic tensor to \mathbb{C} :

$$\begin{cases} \kappa = \frac{1}{3} \exp\left(\ln(\hat{\mathbb{C}}) : \hat{\mathbb{J}}\right) \\ \mu = \frac{1}{2} \exp\left(\frac{1}{5} \ln(\hat{\mathbb{C}}) : \hat{\mathbb{K}}\right). \end{cases} \quad (\text{B.4})$$

References

- [1] Abaimov SG, Trofimov A, Sergeichev IV, Akhatov IS. Multi-step homogenization in the Mori-Tanaka-Benveniste theory. *Compos Struct* 2019;223:110801.
- [2] American society for Testing, Materials. Standard test method for dynamic Young's modulus, shear modulus, and Poisson's ratio by impulse excitation of vibration. ASTM International, 2002..
- [3] Anal A, Bandyopadhyay T, Das K. Synthesis and characterization of TiB2-reinforced iron-based composites. *J Mater Process Technol* 2006;172:70-6.
- [4] Aparicio-Fernandez R, Springer H, Szczepaniak A, Zhang H, Raabe D. In-situ metal matrix composite steels: Effect of alloying and annealing on morphology, structure and mechanical properties of TiB2 particle containing high modulus steels. *Acta Mater* 2016;107:38-48.
- [5] ARCELOR-Research-group, 2008. Patent EP 1 897 963 A1 Bulletin 2008/11, 20..
- [6] Benveniste Y. A new approach to the application of Mori-Tanaka's theory in composite materials. *Mech Mater* 1987;6:147-57.
- [7] Castaing J, Costa P. Properties and uses of diborides, in: Boron and refractory borides. Springer; 1977. p. 390-412..
- [8] Cha L, Lartigue-Korinek S, Walls M, Mazerolles L. Interface structure and chemistry in a novel steel-based composite Fe-TiB2 obtained by eutectic solidification. *Acta Mater* 2012;60:6382-9.
- [9] Chen R, Li B, Li Y, Liu Z, Long X, Yi H, Wang X, Jiang C, Huang M. Revealing the fatigue crack initiation mechanism of a TiB2-reinforced steel matrix composite. *Int J Fatigue* 2020;130:105276.
- [10] Commisso M, Le Bourlot C, Bonnet F, Zanelatto O, Maire E. Thermo-mechanical characterization of steel-based metal matrix composite reinforced with TiB2 particles using synchrotron X-ray diffraction. *Materialia* 2019;6:100311.
- [11] Dammak M, Gaspérini M, Barbier D. Microstructural evolution of iron based metal-matrix composites submitted to simple shear. *Mater Sci Eng A* 2014;616:123-31.
- [12] Derrien K, Morin L, Gilormini P. Designing isotropic composites reinforced by aligned transversely isotropic particles of spheroidal shape. *Comptes Rendus Mécanique* 2018;346:1123-35.
- [13] Devalan P. Vibrations des structures treillis et plaques. *Techniques de l'ingénieur* 2010.
- [14] Dorhmi K, Morin L, Derrien K, Hadjem-Hamouche Z, Chevalier JP. A homogenization-based damage model for stiffness loss in ductile metal-matrix composites. *J Mech Phys Solids* 2020;137:103812.
- [15] E111-17, 2017. Standard test method for Young's modulus, tangent modulus, and chord modulus. ASTM International, West Conshohocken..
- [16] Eshelby JD. The determination of the elastic field of an ellipsoidal inclusion, and related problems. *Proc R Soc Lond A* 1957;241:376-96.
- [17] Eyre DJ, Milton GW. A fast numerical scheme for computing the response of composites using grid refinement. *Eur Phys J-Appl Phys* 1999;6:41-7.
- [18] Garoz D, Gilabert FA, Sevenois RDB, Spronk SWF, Van Paepegem W. Consistent application of periodic boundary conditions in implicit and explicit finite element simulations of damage in composites. *Compos Part B: Eng* 2019;168:254-66.
- [19] Gasnier JB, Willot F, Trumel H, Jeulin D, Besson J. Thermoelastic properties of microcracked polycrystals. Part I: Adequacy of Fourier-based methods for cracked elastic bodies. *Int J Solids Struct* 2018;155:248-56.
- [20] Gaspérini M, Dammak M, Franciosi P. Stress estimates for particle damage in Fe-TiB2 metal matrix composites from experimental data and simulation. *Eur J Mech-A/Solids* 2017;64:85-98.
- [21] Ghossein E, Lévesque M. A fully automated numerical tool for a comprehensive validation of homogenization models and its application to spherical particles reinforced composites. *Int J Solids Struct* 2012;49:1387-98.

- [22] Ghossein E, Lévesque M. A comprehensive validation of analytical homogenization models: The case of ellipsoidal particles reinforced composites. *Mech Mater* 2014;75:135–50.
- [23] Ghossein E, Lévesque M. Homogenization models for predicting local field statistics in ellipsoidal particles reinforced composites: Comparisons and validations. *Int J Solids Struct* 2015;58:91–105.
- [24] Hadjem-Hamouche Z, Chevalier JP, Cui Y, Bonnet F. Deformation behavior and damage evaluation in a new titanium diboride (TiB₂) steel-based composite. *Steel Res Int* 2012;83:538–45.
- [25] Hadjem-Hamouche Z, Derrien K, Héripré E, Chevalier JP. In-situ experimental and numerical studies of the damage evolution and fracture in a Fe–TiB₂ composite. *Mater Sci Eng: A* 2018;724:594–605.
- [26] Ibrahim I, Mohamed F, Lavernia E. Particulate reinforced metal matrix composites—a review. *J Mater Sci* 1991;26:1137–56.
- [27] Kanit T, Forest S, Galliet I, Mounoury V, Jeulin D. Determination of the size of the representative volume element for random composites: statistical and numerical approach. *Int J Solids Struct* 2003;40:3647–79.
- [28] Lartigue-Korinek S, Walls M, Haneche N, Cha L, Mazerolles L, Bonnet F. Interfaces and defects in a successfully hot-rolled steel-based composite Fe–TiB₂. *Acta Mater* 2015;98:297–305.
- [29] Lord J, Morrell R. Measurement good practice guide no. 98: elastic modulus measurement. *Nat Phys Lab. Report* 2006;41–65.
- [30] Mehrabadi MM, Cowin SC. Eigentensors of linear anisotropic elastic materials. *Quart J Mech Appl Math* 1990;43:15–41.
- [31] Michel JC, Moulinec H, Suquet P. A computational scheme for linear and nonlinear composites with arbitrary phase contrast. *Int J Numer Meth Eng* 2001;52:139–60.
- [32] Moakher M, Norris AN. The closest elastic tensor of arbitrary symmetry to an elasticity tensor of lower symmetry. *J Elast* 2006;85:215–63.
- [33] Monchiet V, Bonnet G. A polarization-based FFT iterative scheme for computing the effective properties of elastic composites with arbitrary contrast. *Int J Numer Meth Eng* 2012;89:1419–36.
- [34] Mori T, Tanaka K. Average stress in matrix and average elastic energy of materials with misfitting inclusions. *Acta Metallur* 1973;21:571–4.
- [35] Morin L, Gilormini P, Derrien K. Generalized Euclidean distances for elasticity tensors. *J Elast* 2020;138:221–32.
- [36] Moulinec H, Suquet P. A numerical method for computing the overall response of nonlinear composites with complex microstructure. *Comput Methods Appl Mech Eng* 1998;157:69–94.
- [37] Nguyen VD, Béchet E, Geuzaine C, Noels L. Imposing periodic boundary condition on arbitrary meshes by polynomial interpolation. *Comput Mater Sci* 2012;55:390–406.
- [38] Okamoto NL, Kusakari M, Tanaka K, Inui H, Otani S. Anisotropic elastic constants and thermal expansivities in monocrystal CrB₂, TiB₂, and ZrB₂. *Acta Mater* 2010;58:76–84.
- [39] Raju G, Basu B, Tak N, Cho S. Temperature dependent hardness and strength properties of TiB₂ with TiSi₂ sinter-aid. *J Eur Ceram Soc* 2009;29:2119–28.
- [40] Sani E, Meucci M, Mercatelli L, Balbo A, Musa C, Licheri R, Orrù R, Cao G. Titanium diboride ceramics for solar thermal absorbers. *Sol Energy Mater Sol Cells* 2017;169:313–9.
- [41] Spinner S, Reichard T, Tefft W. A comparison of experimental and theoretical relations between Young's modulus and the flexural and longitudinal resonance frequencies of uniform bars. *J Res Natl Bur Stand Sect A* 1960;64:147–55.
- [42] Springer H, Fernandez RA, Duarte MJ, Kostka A, Raabe D. Microstructure refinement for high modulus in-situ metal matrix composite steels via controlled solidification of the system Fe–TiB₂. *Acta Mater* 2015;96:47–56.
- [43] Szczepaniak A, Springer H, Aparicio-Fernández R, Baron C, Raabe D. Strengthening Fe–TiB₂ based high modulus steels by precipitations. *Mater Des* 2017;124:183–93.
- [44] Tian W, Qi L, Su C, Liang J, Zhou J. Numerical evaluation on mechanical properties of short-fiber-reinforced metal matrix composites: Two-step mean-field homogenization procedure. *Compos Struct* 2016;139:96–103.
- [45] Tian W, Qi L, Chao X, Liang J, Fu M. Periodic boundary condition and its numerical implementation algorithm for the evaluation of effective mechanical properties of the composites with complicated micro-structures. *Compos Part B: Eng* 2019;162:1–10.
- [46] Timoshenko SP. X. On the transverse vibrations of bars of uniform cross-section. *London, Edinburgh, Dublin Philos Magazine J Sci* 1922;43:125–31.
- [47] Torquato S. Random heterogeneous materials: microstructure and macroscopic properties. *Interdisciplinary applied mathematics*. New York: Springer-Verlag; 2002.
- [48] Wang D, Shanthraj P, Springer H, Raabe D. Particle-induced damage in Fe–TiB₂ high stiffness metal matrix composite steels. *Mater Des* 2018;160:557–71.
- [49] Zhan JM, Yao XH, Han F. An approach of peridynamic modeling associated with molecular dynamics for fracture simulation of particle reinforced metal matrix composites. *Compos Struct* 2020;250:112613.
- [50] Zhang JF, Andrä H, Zhang XX, Wang QZ, Xiao BL, Ma ZY. An enhanced finite element model considering multi strengthening and damage mechanisms in particle reinforced metal matrix composites. *Compos Struct* 2019;226:111281.
- [51] Zhang H, Springer H, Aparicio-Fernandez R, Raabe D. Improving the mechanical properties of Fe–TiB₂ high modulus steels through controlled solidification processes. *Acta Mater* 2016;118:187–95.
- [52] Zhang XX, Xiao BL, Andrä H, Ma ZY. Homogenization of the average thermo-elastoplastic properties of particle reinforced metal matrix composites: The minimum representative volume element size. *Compos Struct* 2014;113:459–68.